Magnetic shielding materials for electric vehicles

Tatiana Damatopoulou[1], Spyridon Angelopoulos[1], Aphrodite Ktena[2], Peter Svec[3], Athanasios Mamalis[4], Evangelos Hristoforou[1]

[1]Laboratory of Electronic Sensors, National Technical University of Athens, Zografou Campus, Athens 15780, Greece
[2]National Kapodistrian University of Athens, Greece
[3]Slovak Academy of Sciences, Bratislava, Slovakia
[4]Project Center for Nanotechnology and Advanced Engineering (PC-NAE), NCSR Demokritos, Athens, 15310, Greece

The magnetic field shielding ability of different categories of soft magnetic materials in electric vehicles is discussed in this paper. These materials are magnetically soft steel sheets of a thickness in the order of 1 mm including the structural low carbon steel sheets, Ni3Fe permalloy coatings of a typical thickness in the order of 1 □m, as well as Fe-B amorphous ribbons of 25 □m thickness. Their geometry determines the different magnetic characterization in terms of determining the permeability or magnetization loops. The first one is related to the single sheet testing principle, suitable for steel sheets. The second is a Hall effect based measurement, suitable for thin films, while the third method is related to the magnetostrictive delay line principle. In parallel to the magnetic characterization, structural characterization is also realized, by means of X-ray diffraction, transmission electron microscopy and thermal differential analysis, in order to correlate magnetic properties with structure for property tailoring reasons. This is the methodology for testing the affordable applicability of such types of magnetic materials in magnetic field shielding in electric vehicles.

Keywords: Electric Vehicles, magnetic shielding, magnetic materials.

1. Introduction

The need for electric vehicle shielding is profound, according to international regulations. The upper limits of electric and magnetic field allowable in electric vehicles are the same like in working and living areas and are illustrated in Table 1 [1].

Table 1. The limits of electric & magnetic fields (50 Hz) for human body according to ICNIRP and IEEE.

Organization	**Limits**	
	General public	Occupational
ICNIRP (2010) for 50 Hz	5 kV/m 200 μT	10 kV/m 1000 μT
ICNIRP (1998) for 50 Hz	5 kV/m 100 μT	10 kV/m 500 μT
ICNIRP (1998) for 60 Hz	4.2 kV/m 83 μT	8.3 kV/m 420 μT
IEEE (2019) for 50 / 60 Hz	5 kV/m 904 μT	20 kV/m 2710 μT

Electric field shielding caused by supplying voltages is not an issue, since it is successfully achieved by metallic sheets or coatings [2].

However, shielding against currents and particularly against switching currents may be important for the safety of the driver and the passengers, due to the magnetic fields caused by them. Magnetic field shielding, magnetic shielding for short, is practically realized by either eddy currents screening the penetrating magnetic field, or by soft magnetic materials, trapping magnetic lines [3].

In this paper, the affordable ability of different magnetic materials to trap magnetic field is investigated. Magnetic field trapping is achieved by soft magnetic materials: the more magnetically softer they are, the more magnetic field or magnetic lines can be trapped [4]. These materials can be either soft magnetic steel sheets, including low carbon steels, or permalloy coatings or amorphous ribbons [5].

In the following Chapter 2, the characterization methods are illustrated, concerning magnetic and structural properties. Concerning magnetic properties, emphasis is paid to differential permeability measurements, since it is the property governing the magnetic lines trapping ability. Structural properties are related to transmission electron microscopy and X-ray diffraction studies. Structural characterization aids in improving and tailoring the magnetic properties (differential permeability), to achieve the required shielding properties. These properties are correlated with X-ray diffraction [6], transmission electron microscopy [7] and differential thermal analysis [8].

Chapter 3 is dedicated to the characterization of soft magnetic sheets, including low carbon sheets, of a thickness in the order of 1 mm, while Chapter 4 refers to the characterization of thin Ni3Fe permalloy coatings, in the order of 1 □m. Chapter 5 is related to the characteristics of amorphous ribbons in the form of Fe100-xBx of a thickness of 25 □m with x=12, 15, 17, 20 and 25. Finally the magnetic characteristics of these three different categories are discussed in Chapter 6, targeting the possibility of their affordable use in magnetic shielding.

2. Techniques of magnetic characterization

Three main techniques were used for magnetic properties characterization, the rather classic inductive measurement, the Hall effect measurement and the magnetostrictive delay line (MDL) measurement.

2.1. Inductive measurement of quasi-static magnetization loop

The measurement arrangement is based on the principles of the technical characterization of a single sheet tester (single sheet tester) [9]. The device can measure magnetic hysteresis loops at frequencies from 10 mHz to 10 Hz, with field strengths from 10 A/m up to 10 kA/m, with a resolution of 0.1 A/m. Calibration of the device is based on inter-laboratory comparison of hysteresis loops of materials with known characteristics. The measurement technique is based on the principle of the closed magnetic circuit, where the receiving coil is wrapped around the material to be measured while the excitation is imposed by a coil that surrounds the sample to be measured itself. Two yoke devices are used to close the magnetic circuit of the steel sheet, as shown in Figure 1.

Exciting and receiving the response with a coil applied to the material under test and such a closed magnetic circuit to avoid deflection of magnetic lines outside it allows the field to be calculated accurately. Field application of the method cannot be performed with the aforementioned setup, but it is sufficient to accurately and reliably characterize the soft magnetic material. The electronic part of the setup (Figure 1) includes a NI PXI system with a data acquisition card (DAQ), a bipolar current amplifier with ±70 V, ±6 A characteristics from Kepco, a lock-in amplifier, a signal generator from Hameg, a Hall sensor to measure the field at the surface of the material.

The excitation signal (Figure 2) is created through a function from Matlab with the option of selecting the desired amplitude and frequency values (by the user), while at the same time the characteristics (number of points, trigger activation time, etc.) of the signal generation specify from the card.

The signal is sent to a current amplifier (Kepco) which feeds the excitation coil while a second coil is inserted between them, which acts as a low-pass filter. The signal from the receiving coil (of the order of mV) is received from the card directly or after a small gain preamplification (Figure 2). The signals of the excitation current and the response of the Hall sensor are also received from the card. Digital filtering, integration and determination of the hysteresis loop are performed using Matlab (Figure 3). The quality of the hysteresis loop is acceptable from 10 mHz, considering its repeatability, its symmetry, and its closure at its two extreme values.

The measuring system involves a demagnetization possibility by stimulation the testing magnetic material with a sinusoid shape of a constantly decreasing width. Finally, the system has the capacity of automated measurements by either changing the frequency or the width of the signal, with the possibility of carrying out the necessary demagnetization separately in each step. To define the real magnitude of the excitation magnetic field the following equations can be used:

$$H = \frac{NI}{(L_1+L_2)} \tag{1}$$

where N is the number of turns of the coil, I the excitation coil current, and (L1, L2) the length of the characterization material and the length of the two magnetic materials trapping the magnetic lines consequently. Following tests that took place inside the solenoid having help from a Hall field sensor (with a sensitivity 2.5 mV/Gauss), it was noted that the real field magnitudes were equal to the solutions of equation (1). The following procedure of defining the excitation field, in every case of a closed magnetic circuit, was performed according to equation (1).

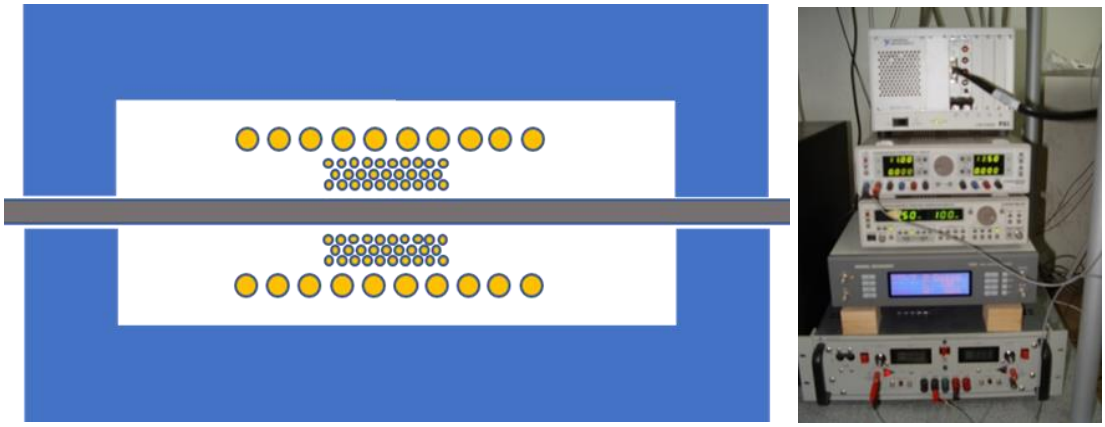

Figure 1. The characterization arrangement of a single steel sheet. The electro-magnetic measurement system (left) and the electronic stimulation and measurement instruments (right).

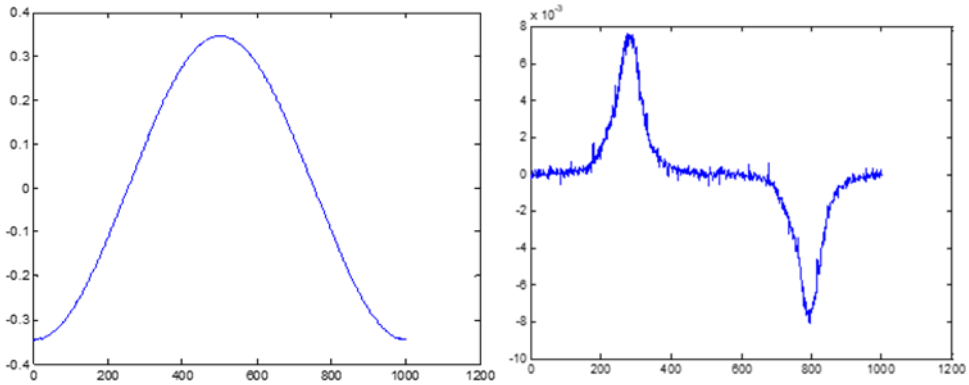

Figure 2. Typical excitation (left) and output (right) of the measurement setup.

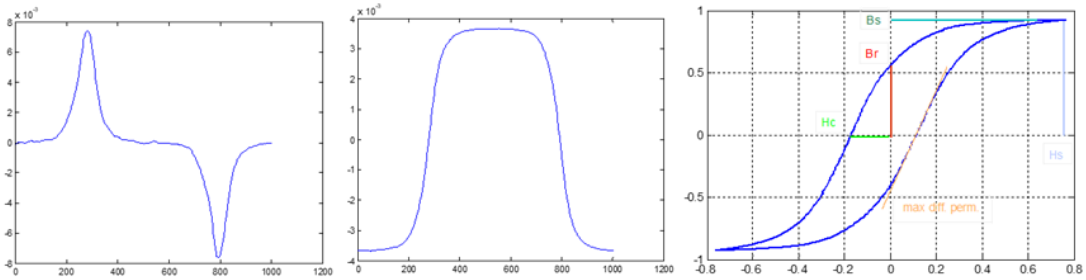

Figure 3. Typical receiving signal after filtering (left), digital integration of the receiving signal (center) and produced hysteresis loop (right).

To calculate the magnetic induction of the tested material, the inductive response formulas of the magnetic flux are used, which are based on Faraday's law of electromagnetic induction and depend the voltage created in the circuit on the rate of change of magnetic flux:

$$V = -N\frac{d\Phi}{dt} \quad (2)$$

given A the cross-section of the sample and N the turns of the coil the result is:

$$V = -NA\frac{d\mathrm{B}}{dt} \quad (3)$$

When the receiving coil remains stationary the magnetic induction is calculated from the integration of the receiving coil output voltage over time:

$$B = -\frac{1}{NA}\int V dt \quad (4)$$

The DC voltage component due to the digital integration is corrected by a constant numerical value which is subtracted from the integral value.
The reliability factors of magnetic measurements are:

- The degree of filling of the receiving coils: the receiving coils must be as close as possible to the magnetic material under measurement
- The leakage of magnetic lines from the magnetizing circuit: care is required for a closed magnetic circuit, even with the use of magnetic fluids (magnetic particles in oleic acid)
- The minimization of the excitation frequency: the lower the frequency, the lower the participation of eddy currents in the induction voltage of the receiving coil. The threshold is the signal-to-noise ratio that decreases as the frequency decreases. The minimum frequency achieved is 0.1 Hz. Dealing with the magnetic viscosity effect is also related to the frequency and it concerns the mobility of the magnetic walls. And in this case the frequency should be as low as possible.

2.2. Hall effect measurement

In order to measure the hysteresis loop of thin sheets of soft magnetic materials and thin films, another setup was developed, which offered reliable results, comparable to the single sheet test or the electromagnetic yoke principe and can be used where the latter cannot for reasons of material geometry or substrate. For example, there are permalloy film deposition arrangements where it is not possible to make the primary and secondary winding around the material. In this case, and to obtain a correct measurement of the hysteresis loop the under test material is placed inside a Helmholtz coil arrangement for homogeneous magnetization purposes with a supply of either dc or quasi-dc current. Hall sensors are placed at the ends of the film or coating or thin steel sheet under measurement above and below the material as shown schematically in Figure 4.

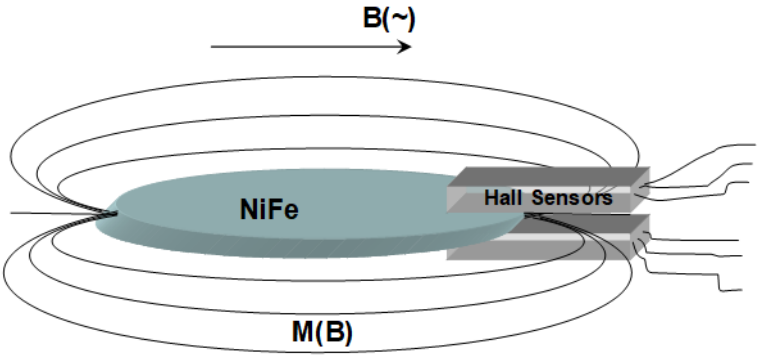

Figure 4. Schematic illustration of the technique for measuring and determining the hysteresis loop of magnetic thin films.

Due to the location of the Hall sensors the magnetic lines exiting the magnetic material return to the antidiametric side of the material. In this way it is possible to exploit the effect of demagnetization to measure the magnetization of the material: the magnetic lines that exit the magnetic material, passing above and below the material, also pass through the Hall sensors with the result that their output voltage is proportional to the field that penetrates them. It is emphasized that the magnetic lines of the excitation field, being parallel to the Hall measurement plane, did not contribute to their measurement. The removal of the Hall sensors from the geometric limit of the material reduces the magnetic field passing through them, until this field is zero. Field zero in this case is the field value below which the sensitivity of the Hall sensor does not allow measurement, which in the case of the device in question is 1 μT. Thus, the sum of the in situ magnetic fields at discrete positions of the Hall sensor can give the internal magnetization of the material to be characterized.

This summation carries the risk of multiple measurement or non-measurement of magnetic lines and in any case, the recommended method of measuring the magnetization is to compare with a transfer standard, i.e., with a magnetic film of a certified magnetizing loop. This way, the measurement of the certified sample allows the measurement's correction by a first-order linear approximation:

$$M_{xi}(H_i) = aM_{ci}(H_i) \tag{5}$$

where H_i the value of the magnetizing field, which is calculated from the value of the field produced by the Helmholtz coils

$$B = 0{,}71\mu_o \frac{nI}{\mathrm{R}} \tag{6}$$

and $M_{xi}(H_i)$ the equivalent measured magnetization value from the Hall sensors and $M_{ci}(H_i)$ the reference value of the magnetization of the certified reference material for the given field H_i.

An indicative measurement of such a field is given in Figure 5, where the reference material (transfer standard) was nickel foil certified at NIST (National Institute for Standards & Technology). The correction factor of the response of the Hall sensor for placing it 1 mm above and below and 1 mm away from the material under measurement was α=2.45 in our experiments.

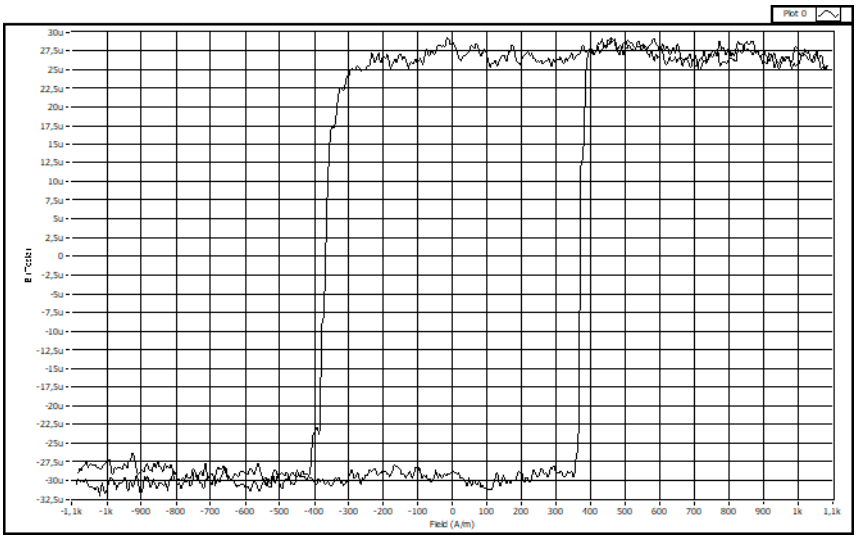

Figure 5. Typical magnetization curve based on the measurement configuration of Figure 4 on a Ni80Fe20 stoichiometry film on the easy magnetization axis.

With this arrangement it is possible to measure the magnetization loop in different anisotropy axes. As a result, the anisotropy of the soft "two-dimensional" magnetic material in different axes on its plane can be found and calculated. This information is valuable in determining the optimal placement of the material in relation to the intended application, both for the shielding needs of this research and for use in other applications such as electric motor development. An example of magnetization measurement on a hard axis of anisotropy is given in Figure 6.

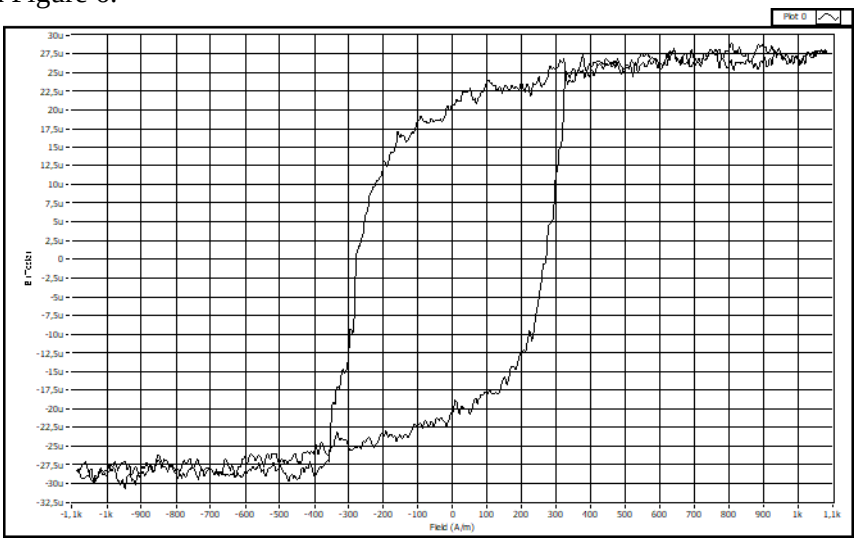

Figure 6. Typical magnetization curve based on the measurement configuration of Figure 4 on a Ni80Fe20 stoichiometry film on hard magnet axis.

2.3. Measurement with magnetostrictive delay lines

The basic arrangement of the magnetostrictive delay line consists of a short excitation coil and a reception coil. The two coils are placed at a distance greater than 5 cm along a

magnetostrictive material of a uniform cross-section (Figure 7).

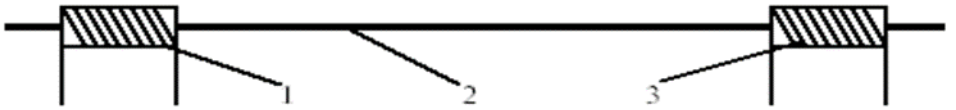

Figure 7. Magnetosrictive delay line: (1) excitation coil, (2) MDL, (3) receiving coil.

The transmission of pulsating current $He(t)$ in the excitation coil induces a pulsating magnetic field along the axis of the magnetostrictive material. Consequently, a dynamic elongation $\delta(t)$ is induced in the volume of the material inside the excitation coil due to the magnetostrictive effect. The uniform cross-section of this material allows the longitudinal transmission of the dynamic elongation $\delta(t)$ as an elastic pulse in the two directions defined by the geometry of the material in question. Thus, the dynamic elongation $\delta(t)$ travels in the magnetostrictive material locally altering the magnetic flux density in the material due to the reverse magnetostriction effect. Thus, it is possible to measure the change in the magnetic field in specific volumes of this material using a reception coil. In classical magnetoelastic materials the optimal range of the pulse field is of the order of 1-3 μs. In this way, the wavelength of the propagating elastic wave is of the order of several mm (the longitudinal speed of sound in ferrous alloys is of the order of 5 km/s). Therefore, since the cross-section of the MDL is ~0.1 mm2, the propagating wave is Lamb-type. A typical reception coil response is given in Figure 8, where the time delay of the received signal is due to and depends on the longitudinal speed of sound.

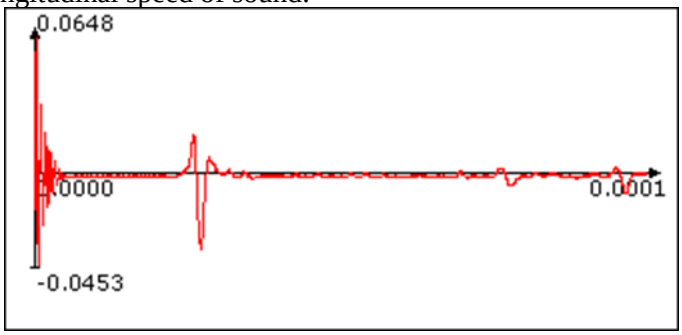

Figure 8. Pulse output voltage versus time. The first high-frequency output voltage (burst) is due to the pulsed excitation field and its coupling with the receiving coil. Next is the main pulse output voltage. The small waveforms following the main pulse output are reflections of the propagating elastic pulse at the ends of the MDL (voltage and time values are given in V and s respectively).

This arrangement is called a magnetostrictive delay line (MDL). Along its path the propagating elastic wave changes the local magnetic component along the MDL, provided that the MDL is locally magnetized. Consequently, the magnetic field in the region of the receiving coil determines the magnetic polarity field and the magnitude of the magnetic flux density is proportional to the output voltage. Thus, the output voltage is proportional to the first derivative of the magnetic flux density and therefore proportional to the magnetic permeability $\mu(t)$. In this way, the magnetic hysteresis loop of the magnetostrictive material at different points is calculated. Material measurement can be implemented on materials in ribbon or fiber form. To measure permeability in two-dimensional materials the setup given

in Figure 9 must be used.

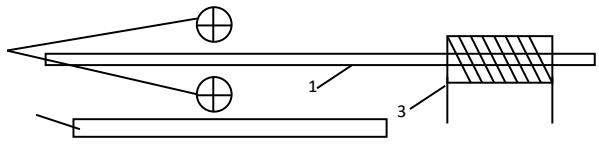

Figure 9. The proposed symmetrical MDL - conductors arrangement: (1) MDL, (2) Pulse current conductors, (3) Receiving coil, (4) Ferromagnetic material under test.

Two pulse current conductors are symmetrically placed above and below the MDL, which is free from mechanical stresses. A pulsating current Ie is transmitted in the same direction in both conductors. In the absence of any other magnetic body in this region of the MDL the magnetic fluxes of the two conductors cancel each other and, consequently, the absence of a pulsating field results in the non-generation of an elastic wave, which in turn does not generate a pulsating output voltage (actually, slight variations in the magnetic flux and mainly in the geometry of the arrangement allow the creation of low pulsed output voltages at the limits of the effective activation distance of the MDL).

Oppositely, the presence of a ferromagnetic material either above or below the conductor arrangement – MDL will affect the magnetic symmetry. This is due to the partial leakage of magnetic lines originating from the conductor located on the other side of the MDL (the boundary condition of the presence of the conductor does not allow a significant amount of magnetic flux of the other conductor to escape). This asymmetry creates an elastic wave that is transmitted inside the MDL and results in a pulsating voltage at the ends of the receiving coil. The amount of magnetic leakage from the MDL to the ferromagnetic material, and consequently the resulting output voltage $V0$, depends on the magnetic permeability of the ferromagnetic material, the distance between the pulse current conductors, as well as the lift-off distance between the MDL and ferromagnetic material. Thus, considering the pulse conductor – MDL arrangement as given with respect to relative conductor and MDL distances and keeping the distance between MDL and ferromagnetic material constant, the pulse output voltage of the MDL depends on the magnetic permeability of the ferromagnetic material. Considering that only the surface of the ferromagnetic material under test practically participates in the magnetic circuit, the obtained pulsed output voltage is related to the surface magnetic permeability of the ferromagnetic material.

Using this arrangement in the absence of another bias magnetic field, which could be generated by an electromagnet, the measured contribution of the surface magnetic permeability of the ferromagnetic material to the pulsed output voltage is caused by the remanent permeability or surface differential magnetic permeability of the remanent magnetization. Thus, random changes of the ambient magnetic field can cause arbitrary changes of the local magnetization and consequently erroneous measurements. This is captured in Figure 10.

This way the magnetic permeability loop can be measured provided that the lift off effect has been minimized or zeroed out. The magnetic permeability loop is associated with the part of the material near the MDL. Thus, it is possible to measure the surface magnetization loop. Also, by moving the MDL-conductor array over the surface of the ferromagnetic material

under test, the uniformity of the local magnetization loops can be determined. The measurements with this method are consistent with the two previous methods of measuring the magnetic permeability.

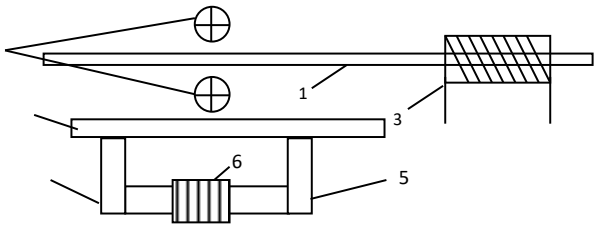

Figure 10. The proposed symmetrical arrangement of MDL - conductors using an electromagnet to create the desired bias field: (1) MDL, (2) Pulsed current conductors, (3) Receiving coil, (4) Ferromagnetic material under test, (5) & (6) Soft magnetic material and excitation coil respectively to create the bias electromagnet.

3. Magnetically shoft steel sheets

The single-phase magnetic materials studied were high-purity ferritic steels, i.e., oriented, and non-oriented electric steels, AISI 1008 steels, as well as Ni3Fe1 alloy (permalloy). These materials were studied as they were manufactured and after thermal annealing and magnetic-thermal annealing. A typical change in the magnetic permeability of electrical steel as produced and after thermomechanical stress is given in Figure 11, where the initial permeability (red line) and the magnetic permeability after thermomechanical fatigue achieved by melting and solidification of the steel (black line) are distinguished. The increase in magnetic permeability due to the voltage field on the measurement axis and in the coercive field of the material can be seen. The magnetic anisotropy of the same (electrical) steel after TIG (tungsten electrode) welding is shown in Figure 12. From these two measurements it becomes clear that it is possible to adapt the magnetic properties to one of the axes of the material.

The value of these measurements has a real meaning when related to the study of the structure and microstructure of steels. In the case of single-phase ferritic steels and permalloy we will emphasize the microstructure analysis i.e., microstructural characterization with TEM, because in this way the existence and density of disorders in the material is demonstrated. With such a measurement, it becomes clear what is needed to improve the magnetic properties of the material, that is, to maximize the magnetic permeability in some or every axis. In this section the analysis of the structure is not presented, since the steels used are single-phase and there is no reason to control their phase, i.e., their structure, because the only thing that can change by such processing is the size and grain orientation.

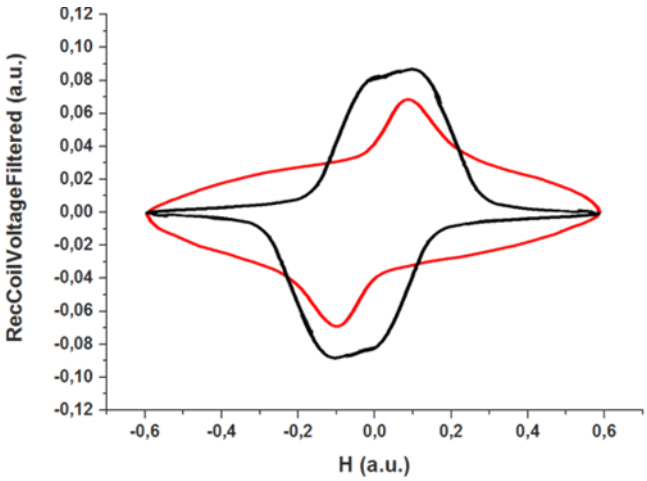

Figure 11. Typical response of as-produced steel (red line) and after thermomechanical fatigue by melting and quenching at a rate of 100 K/s (black line).

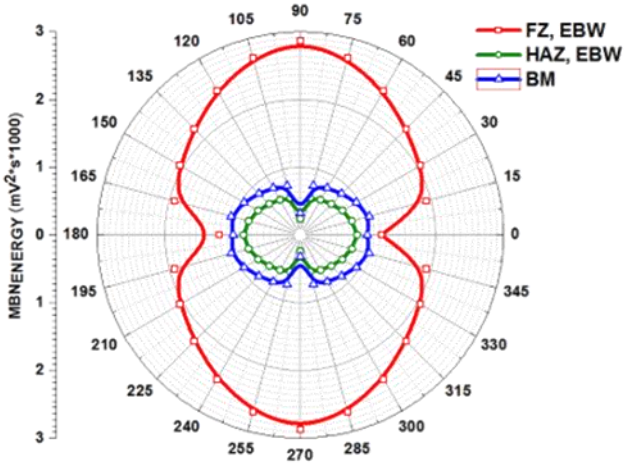

Figure 12. Measurement of magnetic anisotropy of electrical steel after welding. Anisotropy and its change are characteristic, both in the base zone (BM) and the thermally affected zone (HAZ), as well as in the melting zone.

The study of the samples with TEM (JEOL operating at 220 kV) was done to monitor the disorder structures created in AISI 1008 steel after tensile stress and cold rolling in comparison with their microstructure.

Sample preparation includes:

- initial cutting from the samples of each strain with a microtome
- due to the large initial thickness of 2mm, immersion in a strongly acidic environment followed until ~20 μm, where a relatively uniform reduction in thickness was observed (roughness of the order of +1 μm)
- further thickness reduction to drill the characteristic hole in the center of the specimen and gradually increase the thickness of the material using the ion beamer.

Finally, the thickness of the sample under examination was ~5 nm at the boundaries of the hole and ~100 nm at 500 nm away from it. The possible non-systematic errors that may occur during the preparation creating indications that do not correspond to the disorders are:

- the introduction of residual stresses during the stages of chemical attack
- the induction of secondary defects with the appearance of decoration faults from handling the sample when its thickness is small enough, i.e. before and after the use of the ion beamer.

These measurements determine the distribution and density of disturbances in the material due to:

- fluctuation of disturbances in the preparation process
- inability to calculate the density of disturbances due to difficulty in accurately measuring the thickness of the final samples at the point of measurement and
- the point character of measurements in hundreds nm2, which are not completed on the corresponding surface of the material where the magnetic measurements take place (the surface covered by a magnetic measurement is from 1 mm2 to 100 mm2).

TEM measurements have been performed and Figures are illustrated in which disorder structures are depicted for the following samples (in brackets is the percentage of plastic deformation):

- Initial (0%)
- after stretching (5%), (10%) and in the neck area and
- after cold rolling (12.5%), (32.5%) and (62.5%) thickness reduction.

Figure 13 shows the results from the original sample (0% strain), where extremely little distortion is observed indicating that its thermal and mechanical stress history has not resulted in significant distortions and can therefore be used as a reference material for study of the impact of disturbances. These disorders are probably independent of each other. Figure 14 shows results after 5% tensile deformation. In this case, the appearance of areas with more concentrated disturbances is observed. Some decorative disturbances due to incorrect handling of the samples can also be seen. Figure 15 shows results after tensile deformation (10%). In this case, the appearance of areas with more concentrated and denser disturbances is observed, especially in dislocation forests. Distortions of decoration due to incorrect handling of the samples can also be seen here.

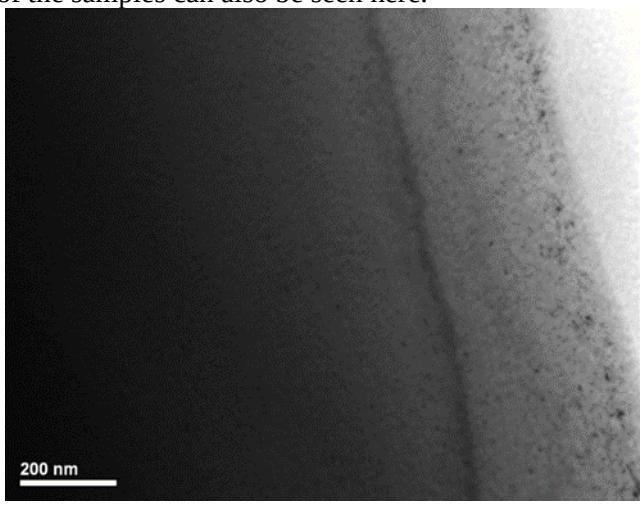

Figure 13. TEM photographs of the original sample (0%).

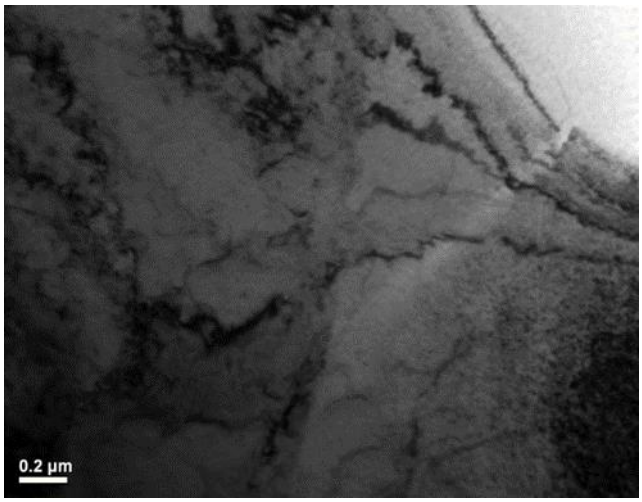

Figure 14. TEM photos of the sample after 5% tensile testing.

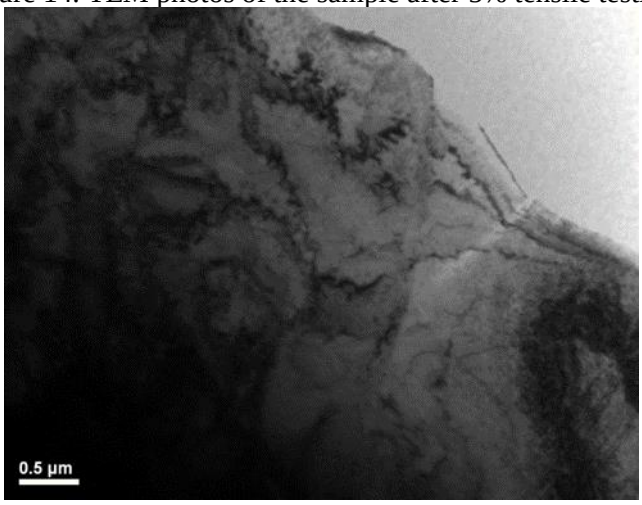

Figure 15. TEM photos of the sample after (10%) tensile testing.

Figure 16 shows results after tensile deformation in the neck region. A stronger occurrence of disturbances and disturbance forests is observed. Decoration disorders are also distinguished.

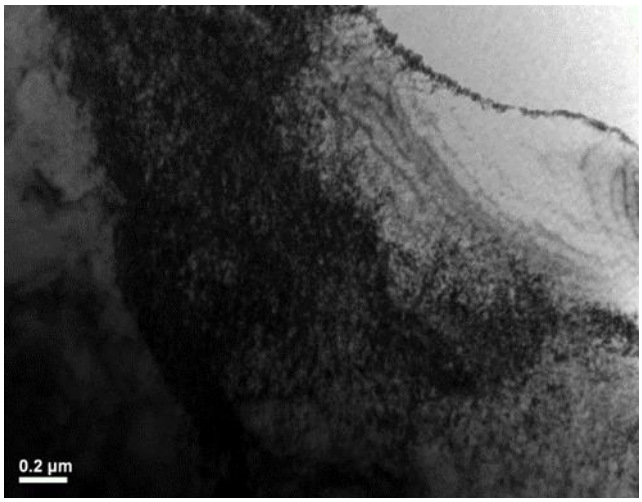

Figure 16. TEM photos of the sample after tensile testing in the neck region.

For the samples with 10% deformation and the one originating from the neck area (Figures 15 and 16) a very increased and ordered distribution of disturbances is found, which shows the uniaxial nature of the fatigue of the material. In any case, the movement of disturbances towards concentration points is observed which will create sub-grain boundaries.

Figure 17 presents results after cold rolling deformation with a thickness reduction of 12.5%. A strong presence of dislocation forests is observed. In the case of rolling, the creation and movement of dislocations is depicted dramatically increased and without being characterized by any strain in their arrangement. Even for 12.5% thickness reduction, local trees and arrays of vertically intersecting dislocations form.

In Figure 18, results are shown after cold rolling deformation with a thickness reduction of 32.5%. The presence of dislocation forests begins to dominate the grain. Figure 19 presents results after cold rolling deformation with a thickness reduction of 62.5%. The presence of dislocation forests starts to produce micro-cracks in the grain.

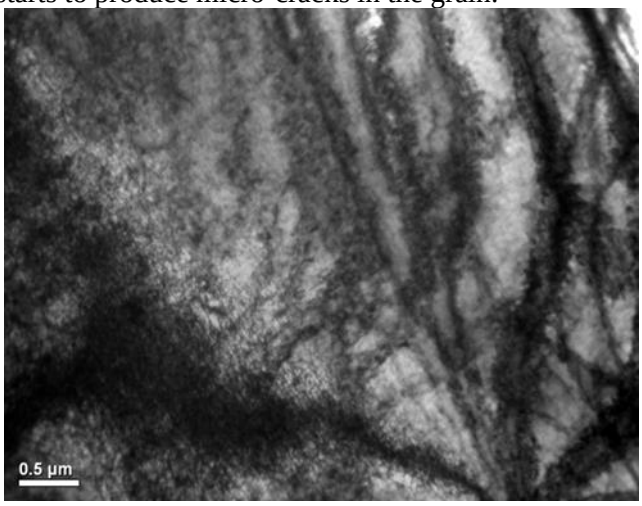

Figure 17. TEM photos of the rolled sample with a thickness reduction of 12.5%.

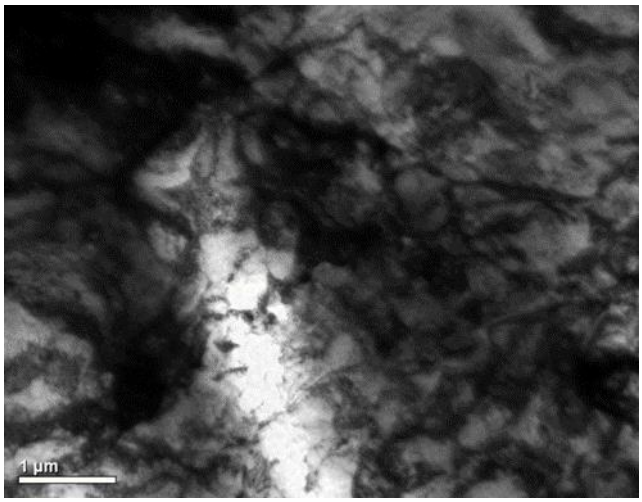

Figure 18. TEM photos of the rolled sample with a thickness reduction of 32.5%.

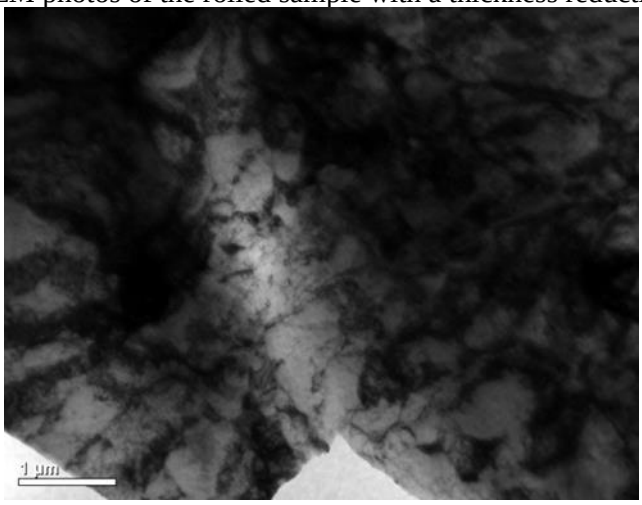

Figure 19. TEM photographs of the as-rolled sample with a thickness reduction of 62.5%.

The difference in dislocation structure and density for the two types of deformation is clearly reflected in the hysteresis loops. In other words, it is proven that the number as well as the arrangement of the dislocations decisively affect the responses of the magnetic measurements.

4. Ni-Fe thin films

FeNi alloys were grown on a sterile and decarburized ferritic steel plate substrate simulating shielding techniques. For the deposition of the alloy in the form of a thin film, the natural vapor deposition method with the sputtering was chosen. It was found that the desired stoichiometric deposition could not be achieved by sputtering.

Thus, it became clear that the most suitable method for preparing the thin films was thermal sublimation and even better deposition with an electron beam (e-gun). According to this method, nickel-iron solid solution alloys were initially created in a vacuum arc oven in the desired proportions by weight. Then in a high vacuum chamber (10-7 mbar) a tungsten wire

produced a lot of electrons. Electrons with properly oriented electromagnets were gathered into a beam and directed onto the solid parent alloy placed in the vacuum chamber. The alloy is locally evaporated where the beam is incident, and the vapors due to the high vacuum adhere to any free surface that exists in a straight line from the evaporation point. Straight above the parent alloy the ferrous substrate is placed. Thus, the material also adheres to the substrate and forms a thin film maintaining the proportions of the parent alloy. A quartz single-crystal piezoelectric sensor was placed next to the substrate connected to a signal generator and an analog-to-digital signal converter to measure the thickness of the deposited film. Figure 20 shows the thermal evaporation and the e-beam aided thermal evaporation, while Figure 21 gives a schematic illustration of the operation of the e-beam.

The magnetic thin films were then characterized to correlate structure and magnetic properties to explain the behavior of the material. Although the nickel-iron alloy has significant magnetic properties the ratio of nickel-iron as a solid solution has been and is a matter of study. One of the goals is to optimize the magnetic permeability of the alloy. Therefore, films of various alloy ratios were developed given in Table 2 (contents by weight).

Figure 20. Physical vapor deposition device by heating the whole of the evaporating alloy in a tantalum crucible (left and left – center). Electron beam physical vapor deposition device (center-right and right).

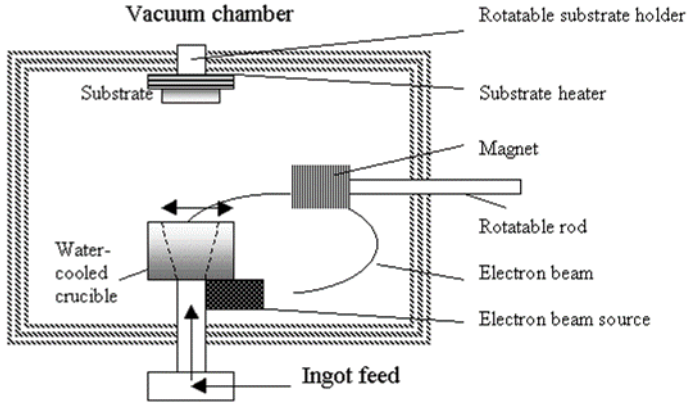

Figure 21. Schematic illustration of thin film deposition method using an electron gun.

Table 2. Alloy ratios by weight of films in nickel and iron

$Ni_{40}Fe_{60}$	$Ni_{60}Fe_{40}$	$Ni_{75}Fe_{25}$	$Ni_{80}Fe_{20}$	$Ni_{85}Fe_{15}$

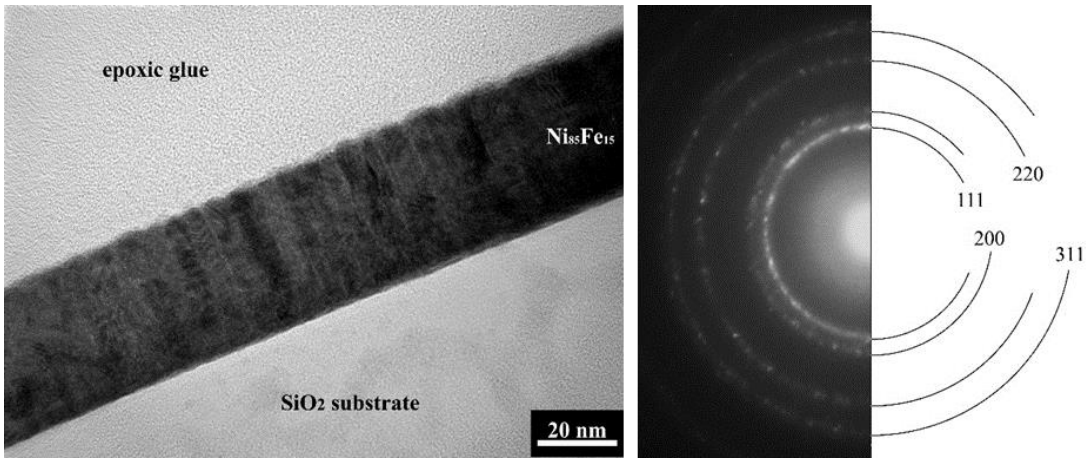

Figure 22. Cross section of a 36 nm thick Ni85Fe15 film where the coexistence of the vertical anisotropy and the anisotropy in the plane of the film can be clearly distinguished (left). Transmitted beam diffraction (right) showing the nano-crystallinity of the film in question as well as its crystallographic axes confirming the orientation of the anisotropy.

In addition to the measurement with the quartz single crystal in real time the thickness of the films was also controlled by measuring the difference in the weight of the substrate before and after deposition on a high-precision scale. The results verified the measurement by the quartz method. A 36 nm thick film was studied by transmission electron microscopy (TEM) and the coexistence of the vertical anisotropy of the structure as well as the in-plane anisotropy is clear (Figure 22). Increasing the thickness of the films guarantees the maintenance of these anisotropic properties.

Additional surface characterization experiments were carried out using the X-ray photoelectron spectroscopy (XPS) method. Using different X-ray emission sources, such as aluminum and magnesium (the aluminum and the magnesium lamps emit at 1486.6 eV and 1253.6 eV respectively) different depths of the material's surface were studied. The results showed that the films have oxidized to a depth of the first 20 – 30 Å of their surface, a logical result as they are in contact with the atmosphere while for greater depths there are minimal oxides. The results from both emission sources are plotted in Figure 23.

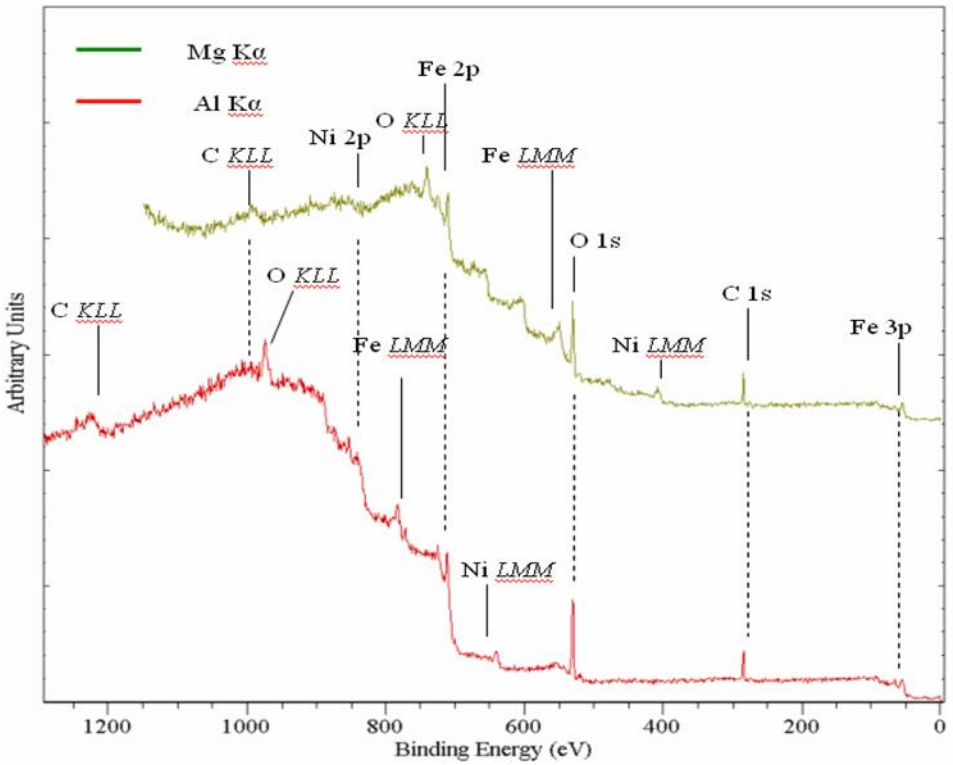

Figure 23. XPS diagram of Ni60Fe40 film.

The magnetic properties of the films define the parameters on which success in shielding against a magnetic field depends. Maximization of magnetization, minimization of coercive force and, finally, isotropy of the material is crucial for shielding against magnetic fields. The direction of the easy magnetization axis was first determined in each sample. With the easy magnetization axis defined the hysteresis loops were defined with a field parallel to the easy magnetization axis and a field perpendicular to it. This made the study of the magnetic properties of the films possible as well as the study of the magnetization energy difference in axial directions.

Typical magnetic hysteresis loops obtained are given in Figures 24a and 24b. The film of said loops is a 100 nm thick Ni80Fe20 alloy. The response of Figure 24a comes from an experiment with a field applied along the easy magnetization axis, while the response of Figure 24b for a field perpendicular to the easy magnetization axis. The coercive field is 367 mA/m, the saturation field of the material is 402 mA/m and the saturation magnetization equals 275.5 mT. The loop is quite square showing a pronounced Barkhousen "jump" from one direction to its antidiametric one. The response shown in Figure 24b is different for the same material. The measured magnitudes are the coherent field equals to 271 A/m and the saturation field of the material is 337 A/m while the saturation magnetization is 275 mT as the previous one. In the case of Figure 24b the external field is imposed perpendicularly to the easy magnetization axis.

In other words, the external field tries to rotate the magnetic dipoles at 900 with respect to their energetically desired position. For this reason, the shape of the loop is not square as

before but sigmoid. This means that a Barkhousen jump does not take place but gradually the dipoles rotate in the direction of the external field. Nevertheless, the material does not show large deviations in its properties (coercive field and saturation field) in relation to the easy magnetization axis.

The magnetic properties and microstructure of the 1-10 μm thick permalloy film were thoroughly studied. It was found that the magnetic permeability exceeds 105 and the coercive field is of the order of mA/m. A typical TEM response is given in Figure 25 showing the crystallinity of the film at such (relatively) large thicknesses. The loop shape of the permalloy was able to provide a large Barkhausen jump with minimal slope after thermal annealing at 380°C in an inert atmosphere for 1 hour and thawing for 24 hours and then magnetic annealing under the same conditions in the presence of a magnetic field of 0.1 T and thrawing in the presence of a field (field cooling).

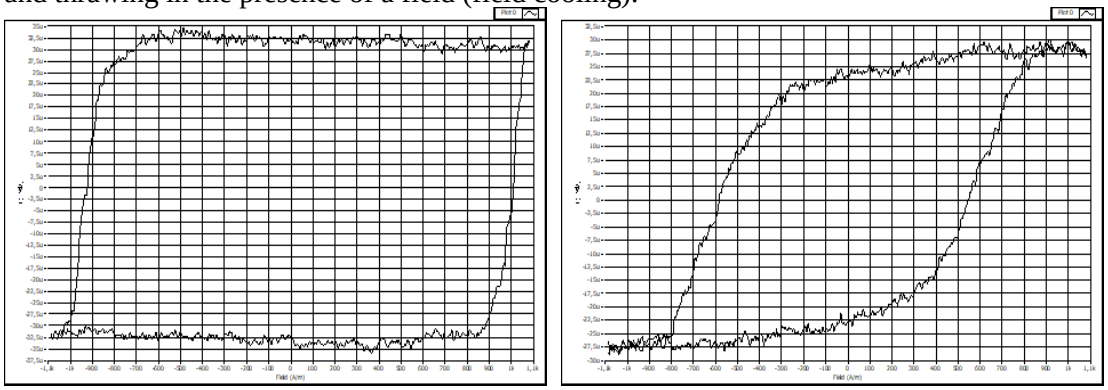

Figure 24. Magnetic hysteresis loops for 93.9 nm thick Ni75Fe25 alloy for imposed field in parallel (a) and perpendicular directions (b) to the easy magnetization axis of the film.

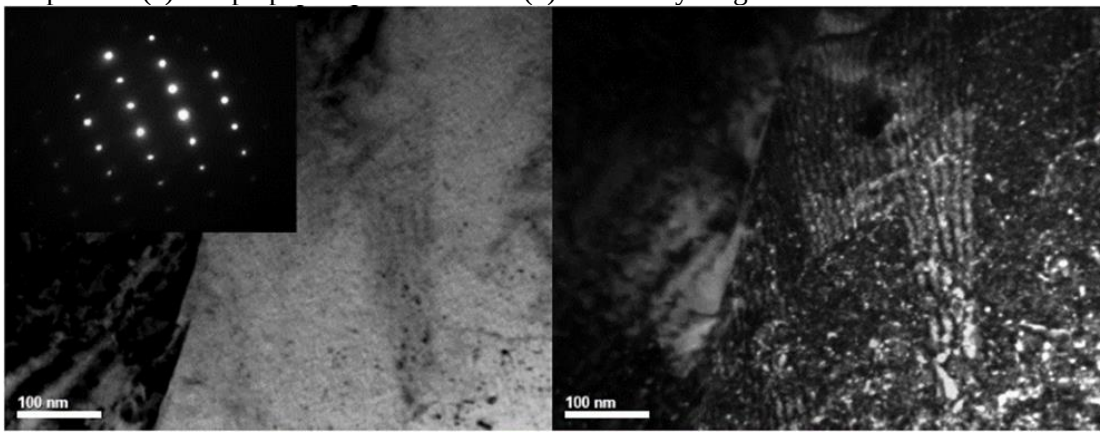

Figure 25. Microstructure of the 10 μm thick Ni3Fe (Permalloy) film as determined by Transmission Electron Microscopy. Bright-field and dark-field micrographs illustrate the presence of relatively limited disorders while the reverse image shows the crystallinity of the film.

5. Amorphous and nanocrystalline shielding materials

Considering the application of amorphous and nanocrystalline materials in energy systems, such as transformers, motors, etc., it appears that their application in the shielding of electric vehicles both in electromobility and charging as well as wireless charging is important. Thus, in this section the materials mentioned will be studied both in relation to their construction and their magnetic and structural characterization. Thus, in this section the materials in question will be studied both in relation to their construction and their magnetic and structural characterization. Specifically, a new family of materials developed by the NTUA Electronic Sensors Laboratory in collaboration with the Metallic Materials Laboratory of the Institute of Physics of the Slovak Academy of Sciences will be examined: the amorphous and nanocrystalline Fe-B films with different boron content from 12% to 25%, thus covering the extended glass formation limit in the subeutectoid compositions up to the supereutectoid limit.

The Fe-B alloys were prepared by planar flow casting in the form of a ribbon 20 μm thick and 6 mm wide approximately. The chemical compositions developed are: Fe75B25, Fe80B20, Fe83B17, Fe86B14 and Fe88B12. The Fe-B eutectic point corresponds to 17% boron, thus dividing the above samples into hypoeutectoid and hypereutectoid. It is known that alloys with boron content of 25% and 20% being the benchmark of the technology can be rapidly quenched in an amorphous phase. In contrast to them, alloys with 14% and 12% boron content have not been prepared and studied so far, being the critical subject of this paper.

The soft magnetic properties of Fe-B alloys were investigated through hysteresis loop measurements before and after annealing. XRD, DSC-TGA and TEM measurements captured the mechanisms of the crystallization process. The crystallization of Fe100-xBx amorphous alloys containing less than 17% boron consists of two crystallization stages. Furthermore, the crystallization and Curie temperature of Fe100-xBx alloys ($12 < x < 25$) were studied. Metal strips having more than 12% boron were found to be completely amorphous while in the as-cast alloy with 12% boron there is a small amount of nanocrystallinity. Each composition was annealed to achieve 5%, 50% and 95% crystallinity. In contrast to crystalline materials, amorphous or glassy materials are characterized by the random arrangement of atoms.

The synthesis of nanocrystalline materials is one of the modern problems in modern materials science. In recent decades interest in this problem has grown dramatically, as it has been found that the properties of nanocrystalline materials change significantly when the crystallite-grain size is reduced below a threshold value. Such changes occur when the average grain size does not exceed 100 nm and are more pronounced when the grain size is less than 10 nm. The chemical composition, microstructure, grain size distribution and, consequently, the properties of nanomaterials are highly dependent on their production method. The physical and chemical properties of nanomaterials differ significantly from those of solid materials of the same composition.

In crystalline materials the coercive field decreases and the magnetic permeability increases with increasing grain diameter D. In rapidly solidified materials with an initially amorphous structure a suitable sequence of atoms is necessary for a subsequent heat treatment to give significantly improved magnetic properties maintaining the size of the nano-grains within the amorphous matrix below about 30 nm. Their improved electrical, optical, physical, chemical,

magnetic and mechanical properties are the motivation for the research done on them while the industrial production and optimization methods are still at a low level.

Many of the important properties of alloys can be explained in terms of crystal order or in many cases in terms of imperfections in the crystal order. An amorphous metal is a metallic material with a metalloid content of ~20% with a disordered structure at the atomic scale. Materials in which such disorder is produced directly from the liquid state on cooling are called "glasses"; thus, amorphous metals are commonly referred to as "metallic glasses" or "glassy metals". Normally, when an alloy is cooled from the liquid state, it can solidify in two ways. If the cooling rate is below some critical rate the liquid may freeze and form a polycrystalline or single-crystalline solid. On the other hand, if the cooling rate is faster than a critical value and at the same time the melting temperature Tm is sufficiently higher than the glass transition temperature Tg, it solidifies into an amorphous structure. The difference in ionic radii of the participating elements is the third parameter that enables the amorphous structure under rapid cooling conditions.

It is difficult to distinguish between truly amorphous solids and crystalline solids in which the crystallite size is very small (less than 2 nm). Even amorphous materials possess short-range order (on length scales of about 1nm), where distinguishing between them is difficult even with the most modern structural characterization techniques. Amorphous alloys were used as precursors to produce nanocrystalline alloys.

The study of nanocrystallization and crystallization of amorphous alloys is achieved by a variety of experimental techniques such as isothermal-linear annealing followed by microstructure observations, electrical resistance measurements, DSC-DTA calorimetric measurements and thermomagnetic analysis in magnetic alloys. These experimental techniques can determine the volume fraction converted to the crystalline phase, as well as the time evolution of this parameter. The basic mechanism of nanocrystallization is the short- or long-range movement of atoms at distances suitable for formation stable cores. The possible ways of transforming the amorphous to crystalline phase are:

Primary crystallization: grains of a crystalline phase with a different chemical composition from that of the amorphous matrix precipitate to form nanocrystalline seeds. Consequently, primary crystallization involves a gradient of its element content in front of the interface of the seed with the remaining amorphous phase, which is enriched in the remaining alloy components. Further crystallization is stopped once metastable equilibrium is reached in the amorphous phase or soft impingement of the seeds. Amorphous residues can crystallize at higher temperatures while the crystalline phase acts as a preferred heterogeneous nucleation site. Growth rates of the seed during primary crystallization are parabolic in time with bulk diffusion (long-range atomic diffusion) being the process-controlling step.

Eutectoid crystallization: two crystalline phases grow simultaneously from the amorphous matrix in a discontinuous reaction. During the transformation there is no difference in concentration on either side of the reaction front. The components separate into two phases within before or after the reaction field, so the growth rates of the eutectic reaction are lower than those of the polymorphic reaction that occurs next. Nucleation growth is controlled by diffusion at the interface and depends on the thickness of the reaction field.

Polymorphic crystallization: involves the formation of a crystalline phase from the amorphous matrix without any change in concentration. The resulting crystallization phase is a supercritical crystalline alloy of a metastable or stable crystalline phase that can later be

transformed by subsequent reactions into more stable phases. This reaction takes place at concentrations close to that of the pure metal or compound. The polymorphic crystallization is massive with large linear growth rates. The mechanism is intermediate between equilibrium reactions and martensitic transformation, i.e., it involves local rearrangement of atoms or groups of atoms in space.

Peritectic crystallization: a stable β phase grows in this reaction at the interface of the metastable phase γ, which exists in the amorphous phase a. The resulting microstructure is particles of phase γ surrounded by a layer of phase b and embedded in phase a. The growth rates are parabolic and decrease with the thickness increasing of the β-phase layer while the process-controlling step is a diffusion through this layer.

The samples used were produced by the Planar Flow Casting (PFC) method, which is the optimal method for rapid cooling of thin films of 25 μm thickness. This casting is the solidification of a melt from a rotating copper wheel that is at room temperature and has high thermal conductivity to achieve a sufficient heat extraction rate. The molten alloy is forced out through a nozzle with the help of inert gas pressure. The melt is drawn off the rotating copper wheel and solidifies to form a thin film. The casting temperature is 150 K-200 K above the melting temperature. The typical thickness of the obtained amorphous metal tape is from 20 μm to 30 μm and the width is 6 mm-10 mm. The adjustment of the casting pressure in the rotating cylinder is done by changing the pressure of the inert gas (Ar). The spurt of radius α is inclined at an angle θ to the tangential plane of the cooling surface and spreads over an area of width w. The rotating copper moves at a speed of 100 km/h creating a 20 μm-25 μm thick ribbon with the same width w. Maintaining the parameters described allows film production. Conversely, failure to meet these parameters leads to film production failure and is reduced to the production of alloy skin usually with polycrystalline microstructure. A similar technique is the “chill block casting” method, which describes a process in which a free spurt of molten alloy impinges on a moving cold substrate, such as a rotating copper drum or rotating water pipe, producing amorphous strips and wires respectively.

G. Herzer found that the dependence of the coercive field on the grain diameter of the nanocrystalline material can be expressed by the sixth power of D [10]. The effect of reducing the overall magnetic anisotropy on magnetic softening is more pronounced in amorphous materials since the absence of medium- or long-range order results in a wider distribution of the local anisotropy axes. In the case of nanocrystalline materials with grain sizes below the ferromagnetic exchange length, relatively more locally concentrated anisotropy axes and statistically larger deviations from the average overall anisotropy result in higher anisotropy than that of the corresponding amorphous alloys. Consequently, the overall anisotropy is a function of the size and volume of the nanocrystalline phase. Moreover, in its nanocrystalline materials derived from partial crystallization of amorphous alloy precursors, the average spacing between nanocrystals is of extreme importance, as the grains are partially coupled to the ferromagnetic element-poor amorphous phase. However, at the same time as the slight magnetic hardening (increase of the coersive field Hc), the partial crystallization of the material results in a significant increase in the average magnetic permeability compared to the corresponding amorphous precursors. Therefore, with an appropriate choice of the alloy composition and the final microstructure, it is possible to optimize the magnetic properties of the nanocrystalline materials.

To determine the nano-crystallization and crystallization temperatures DSC measurements were carried out, which were done at a rate of 10 K/min and performed for all samples. Table 3 gives the nano-crystallization and crystallization temperatures, and Figure 26 plots the DSC response of each of the compositions developed.

These measurements were confirmed by thermo-magneto-gravimetric analysis, which is a complementary method to DSC-DTA and is based on the force of attraction of the magnetic material to be examined by a permanent magnet or electromagnet as a function of temperature; thus, the Curie point (the transition point from the ferromagnetic to the paramagnetic phase) of the examined material can be determined as a function of temperature. Heating takes place at a controlled rate and the temperature changes linearly with time. In this way the comparative change of the force of attraction as a function of temperature is given.

Table 3. Nanocrystallization temperatures Tx and maximum crystallization temperatures.

Composition	Tx(K)	T_{p1}(K)	T_{p2}(K)
$Fe_{75}B_{25}$	689	713	-
$Fe_{80}B_{20}$	688	712	-
$Fe_{83}B_{17}$	685	721	-
$Fe_{86}B_{14}$	643	669	742
$Fe_{88}B_{12}$	577	618	751

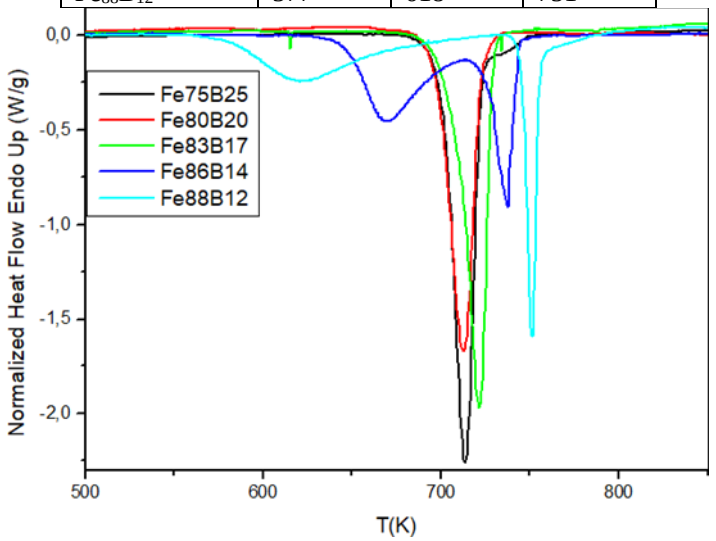

Figure 26. DSC measurements for all samples with linear heating and a rate of 10 K/min.

A permanent magnet is placed under a non-magnetic precision scale used for the measurement. The sample is heated linearly, and the apparent weight measured by the scale is the sum of the real weight of the sample and the magnetic force applied to the sample.

The use of an electromagnet to magnetize the sample allows the magnetic attraction to be interrupted so that the real weight can be confirmed at different temperatures. This setup was developed in the laboratory based on the Perkin Elmer TGS7 thermogravimetric analyzer. Weighing accuracy was 0.1 μg and temperature one ~1K. The autoclave is positioned below and vertically at the sample location.

The balance mechanism is made by adding a non-magnetic diaphragm directly above the autoclave. The autoclave is covered with a thin layer of platinum to maintain the temperature

around the oven and avoid overheating of the thin resistive platinum layer. The temperature of the sample is sensed by a chromel-alumel thermocouple located approximately 1 mm below the platinum sample.

The operating limit of the autoclave is 1100 K, which is quite higher than the temperature requirements of the experiment. The used heating rate was 10 K/min. The weight reading had been tared before the magnetic field was applied to obtain only the magnetic attraction as a measured value. The magnetic force of attraction was ~2.5 mg for each sample.

Figure 27 shows the thermo-magneto-gravimetric measurement as a function of temperature; the weight measurements have been normalized using the initial taring. In this way, the Curie temperature of the amorphous, nanocrystalline, and crystalline phase of each sample was determined and summarized in Table 4. The Curie temperatures of metallic glasses range from 500 K to 800 K and are relatively low compared to their crystalline counterparts. It was observed that an increase in the iron content leads to a decrease in the Curie temperature.

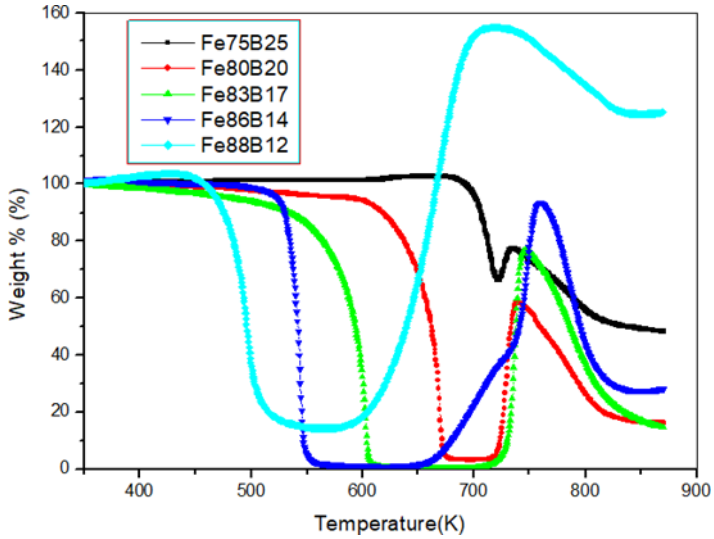

Figure 27. Thermo-magneto-gravitic measurements for each sample.

Table 4. Curie temperature for each composition.

Composition	$Fe_{75}B_{25}$	$Fe_{80}B_{20}$	$Fe_{83}B_{17}$	$Fe_{86}B_{14}$	$Fe_{88}B_{12}$
Tc (K)	709	670	605	553	497

Based on these measurements, which are in relative agreement (always the DSC/DTA measurements are considered reference measurements), it was possible to choose the temperature for the heat treatment of the materials to be nanocrystallized.

Subsequently, after the heat treatment of the samples indicated by DSC/DTA measurements and thermo-magneto-gravimetric measurements, XRD and TEM measurements were performed on the samples that were in an amorphous state (as-cast) and after heat treatment (annealing). The temperatures chosen were the highest in each temperature range (comparative between DSC/DTA and the thermo-magneto-gravitational method).

Figure 28 presents the X-ray diffraction response of the cast films. The characteristic amorphous state response is observed around the α-Fe peak (2θ between 40o-50o). The second peak is also observed (2θ between 70o-90o) around the Fe2B phase. It is confirmed

that all compositions are in the amorphous state except for the composition Fe88B12. In this composition there are small peaks that indicate the presence of nano-crystallinity.
Figures 29, 30, 31, 32 and 33 illustrate the X-ray diffraction before and after annealing at different temperatures (the annealing temperatures are given in K) for the samples Fe75B25, Fe80B20, Fe83B17, Fe86B14 and Fe88B12 respectively. The formation of small crystalline peaks with a spread response range around the maximum of the phase peaks of α-Fe and Fe2B is clearly visible.

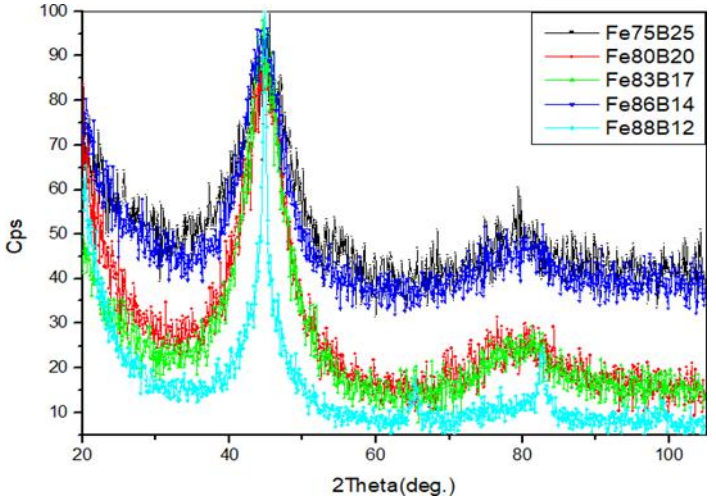

Figure 28. X-ray diffraction for all samples.

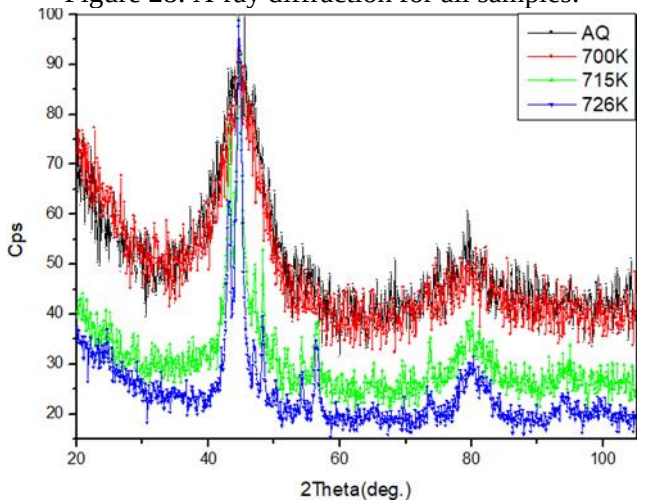

Figure 29. X-ray diffraction for Fe75B25 composition before and after annealing.

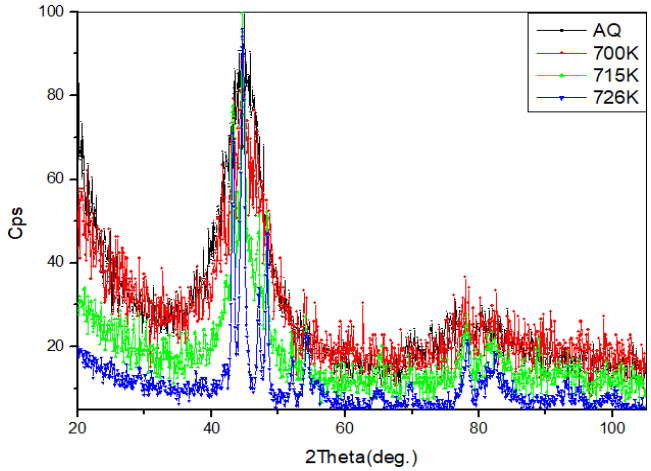

Figure 30. X-ray diffraction for the Fe80B20 composition before and after annealing.

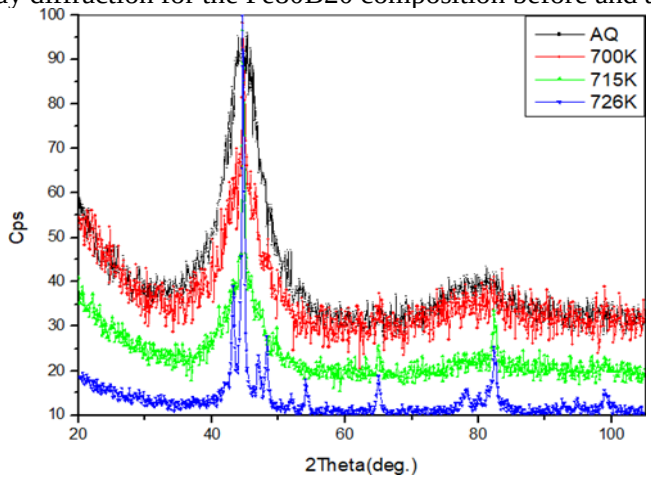

Figure 31. X-ray diffraction for the Fe83B17 composition before and after annealing.

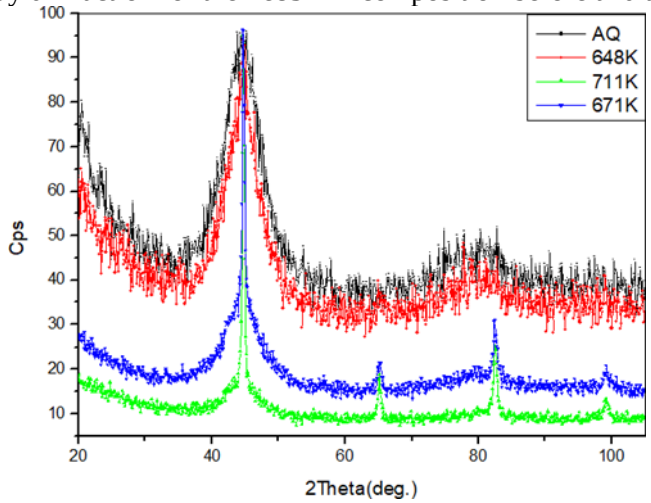

Figure 32. X-ray diffraction for the Fe86B14 composition before and after annealing

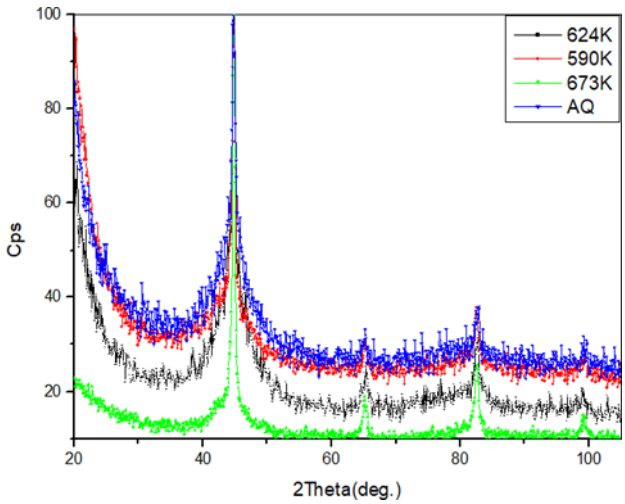

Figure 33. X-ray diffraction for the Fe88B12 composition before and after annealing.

The samples were then characterized by transmission beam electron microscopy (TEM). Figure 34 shows a TEM image for crystallinity percentages of 5%, 50% and 95%. At 5% crystallization, Fe3B crystallites enclosed by an amorphous matrix are observed. At 50% crystallization (715 K) the number and size of crystallites increases. In treatment at 726 K almost total crystallization is observed (95%). At such high percentages of crystallinity the phases are more stable. This is also shown by the electron diffractions (inset). At 5% crystallization the amorphous ring dominates, which weakens in favor of the crystalline phase at 50% crystallization and disappears at 95% crystallization.

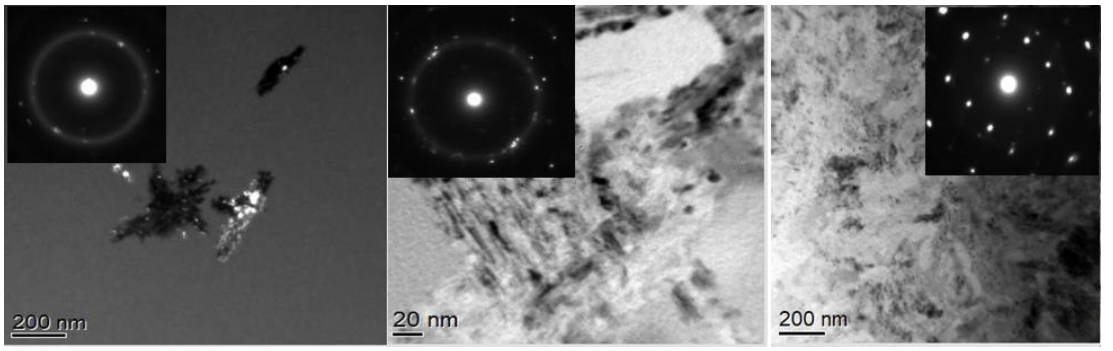

Figure 34. TEM images for the Fe75B25 sample for 5% (left), 50% (center), and 95% (right) crystallinity.

Figure 35 shows the crystallization process in the Fe80B20 sample, where the amorphous state of the sample (left) is confirmed as there are no grains while its crystallization shows eutectic crystallization with α-Fe and Fe3B, which in fact have a spherulite shape.

Figure 36 shows the TEM images of sample Fe83B17, where eutectic crystallization and dendritic growth of the α-Fe phase with tetragonal Fe3B phases are observed. α-Fe grains at 5% crystallinity are approximately 60-80 nm, while at 95% crystallinity they are about 100-150 nm. At a temperature of 700 K (5% crystallinity) there are few nanograins enclosed by the amorphous matrix, while at a temperature of 726 K (95% crystallinity) the volume fractions of the α-Fe and Fe3B phases increase significantly covering over 80% of the

volume.
Figure 37 shows the TEM images of the Fe86B14 sample, where 5% primary crystallization is observed from 648 K (left), while primary crystallization continues at 681 K.
Figure 38 shows the TEM images for the Fe88B12 sample, which was cast as a tape for the first time and in which nanocrystals are observed from the as-cast material before its heat treatment (left). More specifically, spherical α-Fe and Fe2B phase grains are observed, which are enclosed in the amorphous matrix. At higher degrees of crystallinity, the grain size increases, and the α-Fe phase dominates. In fact, at 95% crystallinity, the sample is saturated as the grains cover approximately 85-90% of the sample volume. Similarly to the Fe86B14 composition most grains are α-Fe phase while there are very few Fe2B phases.

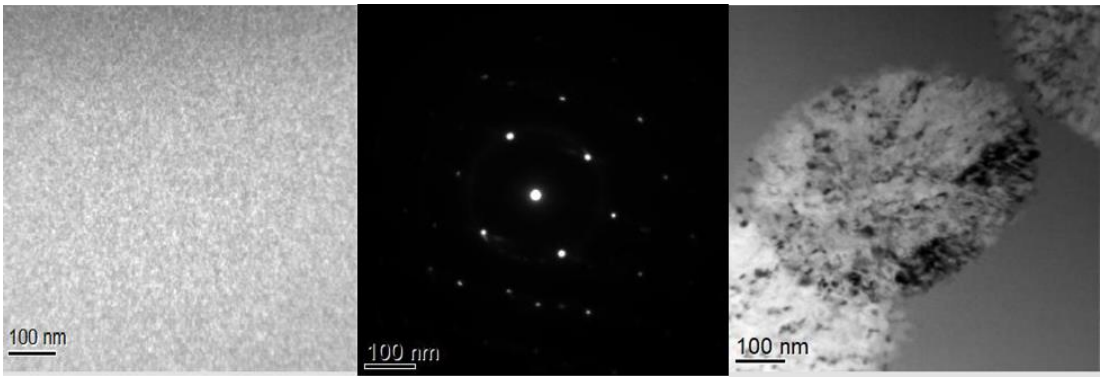

Figure 35. TEM images for the Fe80B20 sample showing the amorphous state in the as-produced sample (left), the crystalline response electron diffraction - SAED (center), and the nanocrystallization (right).

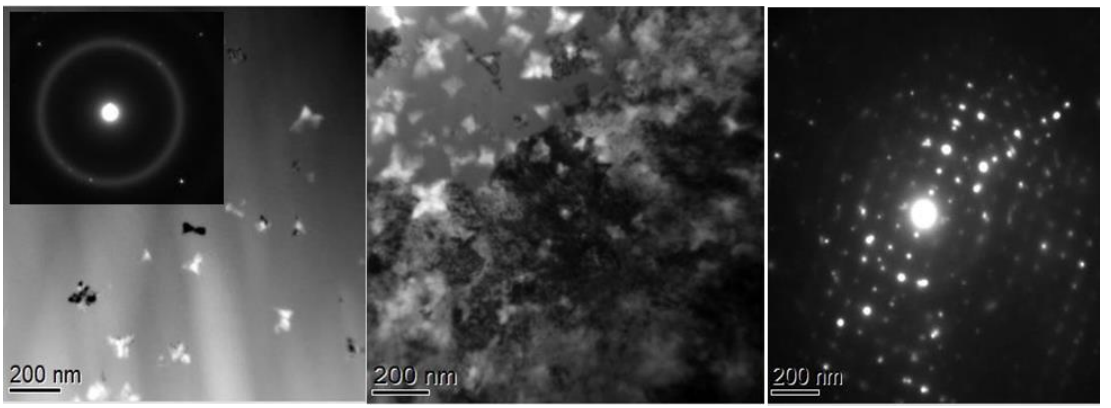

Figure 36. Crystallization process of the Fe83B17 eutectic phase sample, where 5% nanocrystallization is observed at 700 K (left), almost total crystallization at 726 K (center), which is confirmed by electron diffraction (right).

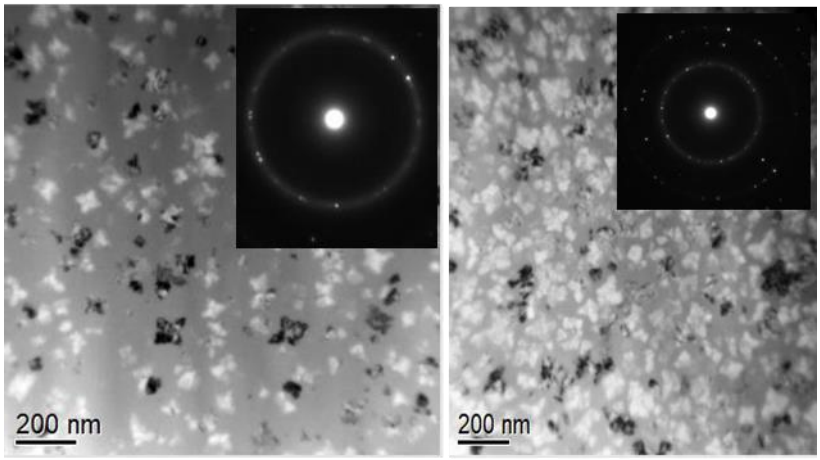

Figure 37. TEM images of sample Fe86B14 with 5% primary crystallization at 648 K (left), which continues at 681 K.

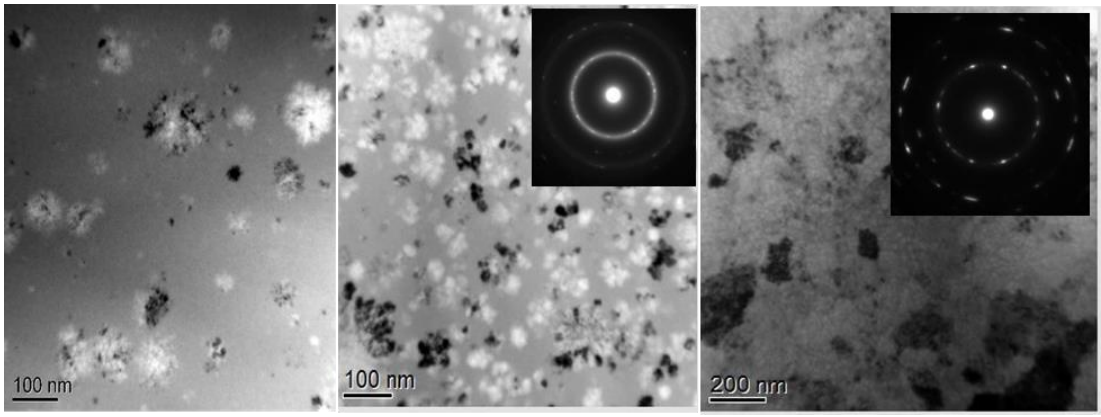

Figure 38. TEM images for sample Fe88B12, in which nanocrystals are observed even in the as-cast material (left); the nanocrystals are enhanced to 50% crystallinity at 590 K (center) and complete crystallization 100% at 671 K.

From the characterization of structure (XRD) and microstructure (TEM) it was observed that:

- The eutectic crystallization is observed in the composition Fe75B25 and Fe80B20 and results in the appearance of α-Fe phases and Fe3B tetragonal phases. At 95% crystallinity a small volume fraction of Fe2B phase appears because at higher temperatures the system transforms into stable phases. The sample is in the so-called metastable equilibrium.
- The 17% boron concentration is the eutectic point in the phase diagram and is therefore also the boundary of sub-eutectoid and super-eutectoid alloys. In this composition eutectic crystallization is observed as in Fe75B25 and Fe80B20 compositions. The phases observed are α-Fe and Fe3B phases and the sample is in metastable equilibrium.
- In the compositions Fe75B14 and Fe80B12 primary crystallization is observed. Crystallization can be summarized by the following solid-state reactions:

$$amorphous\ phase \rightarrow Fe_3B + a - Fe$$

$$Fe_3B \rightarrow Fe_2B + a - Fe$$

$$Fe_2B \rightarrow a - Fe$$

Finally, the magnetic properties were determined using the hysteresis loops measurement of the samples. Measurements were taken using the single sheet tester method. Figure 39 (top) shows the hysteresis loop of the as-cast samples, while Figure 39 (bottom) shows the loops after heat treatment. Magnetic measurements after heat treatment are not ideal as an increase in the coercive field Hc is observed, which is attributed to the strong presence of the Fe2B phase. In any case, Fe88B12 films can be used even as cast, since they have a large saturation magnetization and a controllable small coercive field.

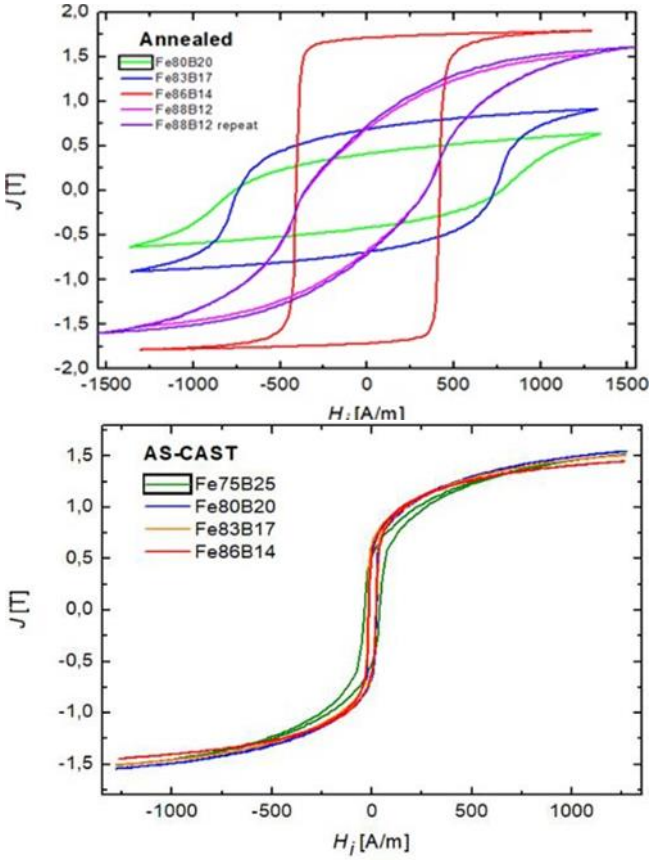

Figure 39. Hysteresis loops of the samples as cast (top) and after heat treatment (bottom).

Conclusions

Three different types of soft magnetic materials for magnetic field shielding have been investigated, mainly illustrarting the magnetic methods to determine their magnetic properties, as well as structural characterization methods to correlate and explain their magnetic properties. The magnetic methods are separated to the single sheet testing method for steel sheet magnetic testing, the Hall type of magnetic loop measurement for thin films, as well as the magnetostrictive delay line technique for ribbons and tapes. The demonstrated

structural characterization methods are the X-ray diffraction, the transmission electron microscopy and the differential temperature analysis. Following these characterization methods, it is possible to determine the proper soft magnetic materials for magnetic field shielding of electric vehicles, following different property tailoring techniques, such as mechanical or thermal treatment.

References

1. Coey, J. M., Magnetism and magnetic materials, Cambridge university press, 2010.
2. C. Kittel and H. Fan, Introduction to solid state physics, American Journal of Physics, 25, pp. 330-330, 2004.
3. Egami T., Flanders P. J., Graham Jr C. D., Low− field magnetic properties of ferromagnetic amorphous alloys, Applied Physics Letters, 26(3), pp. 128-130, 1975.
4. Warlimont H., The impact of amorphous metals on the field of soft magnetic materials, Materials Science and Engineering, 99(1-2), pp. 1-10, 1988.
5. Hilzinger H. R., Recent advances in rapidly solidified soft magnetic materials., Journal of Magnetism and Magnetic Materials, 83(1-3), pp. 370-374, 1990.
6. McHenry M.E., Willard M.A., Laughlin D. E., Amorphous and nanocrystalline materials for applications as soft magnets, Progress in Materials Science, 44(4), pp. 291-433, 1999.
7. Duwez P., Willens R. H., Rapid quenching of liquid alloys, Transactions of the Metallurgical Society of AIME, 227(2), 362, 1963.
8. Cohen M. H., Turnbull D., Composition requirements for glass formation in metallic and ionic systems, Nature, 189(4759), pp. 131-132, 1961.
9. Deanko M., Kepaptsoglou D. M., Muller D., Janickovic D., Skorvanek I., Hristoforou E., Svec P., Identification and quantification of microstructures formed during nanocrystallization of amorphous (Fe, Co) -Nb-(Si, B) systems, Journal of microscopy, 223(3), pp. 260-263, 2006.
10. Herzer G., Grain size dependence of coercivity and permeability in nanocrystalline ferromagnets, IEEE Transactions on magnetics, 26(5), pp. 1397-1402, 1990.